

1 FLARE-ASSOCIATED TYPE III RADIO BURSTS AND DYNAMICS OF THE
2 EUV JET FROM SDO/AIA AND RHESSI OBSERVATIONS

3

4 Naihwa Chen¹, Wing-Huen Ip^{1,2}, and Davina Innes³

5

6 ¹ Graduate Institute of Astronomy, National Central University, Jhongli 32001, Taiwan,

7 R.O.C.

8 d949001@astro.ncu.edu.tw

9 ² Institute of Space Sciences, National Central Univeristy, Jhongli 320001, Taiwan,

10 R.O.C.

11 wingip@astro.ncu.edu.tw

12 ³ Max-Planck-Institut fuer Sonnensystemforschung, 37191, Katlenburg-Lindau,

13 Germany

14 innes@mps.mpg.de

15

16

17

18

19

20

21

22

23

24

25

26

Abstract

27 We present a detailed description of the interrelation between the Type III radio
28 bursts and energetic phenomena associated with the flare activities in Active region
29 AR 11158 at 07:58 UT on 2011, Feb. 15. The timing of the Type-III radio burst
30 measured by the radio wave experiment on the Wind/WAVE and an array of
31 ground-based radio telescopes, coincided with an EUV jet and hard X-ray emission
32 observed by SDO/AIA and RHESSI., respectively. There is clear evidence that the
33 EUV jet shares the same source region as the hard X-ray emission. The temperature of
34 the jet, as determined by multiwavelength measurements of AIA, suggests that type
35 III emission is associated with hot, 7 MK, plasma at the jet's footpoint.

36 Subject heading: Sun: flares --- Sun: X-rays ---Sun: type-III radio bursts

37

38

39

40

41

42

43

44

45

46 **1. Introduction**

47 It is generally believed that energetic activity like solar flares in the solar atmosphere
48 is driven by magnetic reconnection in the vicinity of active regions (ARs). Formation
49 of current sheets due to the emergence of magnetic flux near the boundaries of
50 sunspots could be conducive to reconnection which is characterized by particle
51 acceleration and X-ray jets (Shibata et al. 1992; Shimojo et al. 1996; 1997; 1998). The
52 generation of an electron beam in connection with particle acceleration near the
53 reconnection site leads to a number of impulsive physical phenomena which can in
54 turn be used as diagnostic tools for solar flares. These include the injection of
55 near-relativistic electrons into interplanetary space (Lin 1985; Kahler et al. 2007;
56 Klassen et al. 2011) and the production of Type-III radio bursts with frequencies from
57 a few tens to thousands of kHz by the streaming of low energy electrons (< 30 keV)
58 upward through the corona (Suzuki et al. 1985). These two types of electron
59 signatures have been shown to display very close correlation in time by comparing the
60 radio wave measurements by the SWAVES (Bougeret et al. 2008) and the solar
61 electron and proton telescope (SEPT) observations (Müller-Mellin et al. 2008) on the
62 STEREO spacecraft, and allowing for the travel time of the energetic electrons along
63 the interplanetary magnetic field line (Klassen et al. 2011).

64 The association of Type-III radio bursts with EUV jets was studied by a number of
65 authors (Aurass et al. 1994; Kundu et al. 1994; Kundu et al. 1995; Raulin et al. 1996;
66 Kundu et al. 2001; Pick et al. 2006; Wang et al. 2006; Nitta et al. 2008; Krucker et al.
67 2011). Taking advantage of the multi-wavelength EUV imaging observations of the
68 Solar Dynamic Orbiter (SDO), Innes et al. (2011) recently demonstrated further that
69 Type III radio bursts detected on August 3, 2010, preceded by about 30s onset of
70 narrow EUV jets detected in 211 \AA and 304 \AA in an active region. The correlation of

71 the Type-III radio waves with impulsive hard X-ray (HXR) emission was investigated
72 by Benz et al. (2005a) and Dąbrowski and Benz (2009) by using the Reuven Ramaty
73 High Energy Solar Spectroscopic Imager (RHESSI) (Lin et al. 2002). What is still
74 missing is the direct comparison of all three kinds of data for jets in ARs, so that a
75 more comprehensive picture of the reconnection process can be obtained.

76 Following the approach of these authors, we would like to examine the interrelations
77 among the Type III radio bursts from the Waves/Wind experiment (Bougeret et al.
78 1995), Compact Astronomical Low-cost Low-frequency Instrument for Spectroscopy
79 and Transportable Observatory (e-Callosto) (Benz et al. 2005b) and Phoenix-3 (Benz
80 et al. 2009), the EUV jets from Atmospheric Imaging Assembly (AIA) (Lemen et al.
81 2012) and the HXR emission from for AR11158 between February 13 and 15, 2011.

82 The paper is organized as follows. Section 2 will describe the instruments,
83 observations and data analysis. Section 3 provides an analysis of the dynamical
84 evolution and the interrelation among the Type-III radio bursts, the EUV jet feature
85 and the HXR source region. The thermal evolution of the jet ejecta after the impulsive
86 flare at 07:58 UT is investigated by means of multi-wavelength AIA measurements. A
87 summary and discussion will be given in Section 4.

88

89 **2. Instruments and Observations**

90 AR 11158 was the first active region to appear in the rising phase of the current solar
91 cycle 24. When it crossed the solar disk from the central meridian to the west limb
92 between February 11 and 21, its morphology changed rapidly from simple β - to
93 complex B- β gamma configuration (Tan et al. 2012). A X2.2 flare occurred at 01:33
94 UT on February 15. In total, 56 C-class flares and five M-class flares were produced

95 in AR 11158 between February 13 and 18 (Beauregard et al. 2012). They give us the
96 first opportunity to study the relation between Type III radio bursts and jets associated
97 with flare activity using the new instruments on SDO together with an array of
98 experiments on the GOES, RHESSI, and STEREO spacecraft. In this work, we focus
99 our attention on a C-class flare and EUV jet which took place at 07:58 on February 15,
100 2011.

101 From SDO, we used Helioseismic and Magnetic Imager (HMI) and AIA data. The
102 HMI images the whole solar disk in the photospheric Fe I, absorption line at 6173.3 \AA
103 with an angular resolution of $0.5''$ pxl and a cadence of 45 secs (Schou et al. 2012).
104 AIA observes the full solar disk with an angular resolution of $0.6''$ and a cadence of
105 12 secs in a number of wavelengths which allow to probe the temperature
106 distributions in different regions from transition region to the corona. For example,
107 the 94 \AA filter is centered on the Fe XVIII line emitted by hot plasma with $\log T \sim 6.8$,
108 the 211 \AA filter reveals the regions of warm plasma in the vicinity of ARs at $\log T \sim 6.2$,
109 and the 304 \AA He II line forms in the solar chromosphere and the transition region at
110 $\log T \sim 4.7$. The 131 \AA filter cover both the hot Fe XXI line ($\log T \sim 7$) and cool Fe
111 VIII lines ($\log T \sim 5.6$). As will be discussed later in section 3, the ratios of different
112 line intensities can be used to deduce the plasma temperature.

113 The archived HXR data from RHESSI are another important component of our study.
114 RHESSI images the full Sun in the energy range from 3 keV to 17 MeV with an
115 angular resolution of $2.3''$ providing detailed information on the positions and
116 structures of thermal and non-thermal HXR sources in different energy bands.

117 For radio wave measurements, we have made use of three data sets. The observations
118 of Wind/Waves experiment cover the frequency range between 1 MHz and 14 MHz

119 (Bougeret et al.1995). The frequency range from 45 MHz to 870 MHz with a
120 resolution of 62.5 kHz is covered by the e-Callisto network of solar radio
121 spectrometers. This network is composed of nine stations in different longitudes of
122 global monitoring observations and aims at 24 hours coverage of radio emissions
123 (Benz et al 2005b). Finally, the Phoenix-3 multi-channels radio spectrometer with a
124 5-meter antenna at Bleien observatory, Switzerland has the capability of measuring
125 solar radio emission at frequency range of 1-5 GHz with a spectral resolution of 61
126 kHz and a time resolution of 200 ms (Benz et al. 2009).

127

128 **3. RESULTS**

129 **3.1 RADIO SIGNATURES AND HXR EMISSIONS**

130 The HXR and radio emissions are generally thought to be a signature of particle
131 acceleration. The intensive HXR flux is often accompanied by metric and decimetric
132 emissions in the main phase of a flare (Benz et al. 2005a). Figure 1 shows a
133 comparison of the Type-III radio bursts as observed in different frequency ranges
134 (from 1 MHz to >1 GHz) by the Wind/Wave experiment and ground-based
135 observations (e-Callisto and Phoenix-3). After the first appearance at 07:58 UT, the
136 radio signal drifted fast from a few GHz to very low frequency (~1MHz) within 2
137 minutes. This dynamic behavior is basically due to the outward beaming of mildly
138 relativistic electrons from the flare site to the outer corona and interplanetary space.
139 About 1 min before the main pulse at 07:58 UT, decimetric and metric radio
140 emissions can be found probably indicating pre-flare electron acceleration. At the
141 same time, some faint narrowband spikes at higher decimetric frequency shown in

142 Phoenix-3 spectrum are well associated with the rise of HXR 30-50 keV flux. The
143 generation of decimetric radio bursts is thought to be related to the primary energy
144 release process. Figure 2 compares the dynamic spectra from Wind/Waves with the
145 time profile of HXR fluxes measured by RHESSI and EUV emissions from SDO/AIA,
146 respectively. The intense type III radio burst took place at 07:58 UT which is also the
147 peak time of the HXR fluxes (4-10 keV) but the EUV flux peaks a few seconds later.
148 The near simultaneous occurrences of the Type III radio bursts, EUV and HXR
149 emissions speak for their common origin associated with the impulsive flare. It shows
150 that the energetic electrons accelerated via reconnection can gain immediate access to
151 the outer corona and interplanetary space.

152 Note that the close correlation between decimetric radio pulsations and the HXR
153 emission has been report by Benz, et al. (2005a) and Dąbrowski and Benz (2009). The
154 variations of HXR profiles show the formation of a secondary peak at 08:01 UT in the
155 energy ranges of 4-10 keV and 10-30 keV, but not at the 30-50 keV channel. The
156 absence of a Type III radio burst at the time of the second peak might mean that the
157 generation mechanism responsible for the lower energy HXR's did not produce the
158 required energetic electrons, although, as discussed in the next section, EUV jets were
159 seen. Another possibility is that all accelerated electrons might be directed along
160 closed field lines back to the Sun.

161

162 3.2 RADIO SIGNATURES AND EUV JETTING

163 Figure 3a shows contours of the HMI magnetogram superimposed on the AIA image
164 taken at 211 Å at the time of the peak HXR flux. There are two pairs of sunspots plus

165 a number of smaller magnetic concentrations. Loop-like structures can be found
166 emanating from some of these localized areas. A prominent jet feature appears on the
167 lower left hand side of the figure. This EUV jet has its root in a small region
168 containing two opposite magnetic polarities which might have been responsible for
169 the reconnection. Not specifically shown in Figure 3a is the location of a region of
170 strong HXR emission at the footpoint of the EUV jet which was situated between the
171 two opposite polarity magnetic field concentrations. To trace the time evolution of the
172 EUV jet and the HXR source region, contour maps of the HXR emissions in three
173 different energy channels are aligned and overlaid on the 211 Å images at different
174 times from 07:55 UT to 08:11 UT (as Figure 3b.). It can be seen that the HXR source
175 region was not there at 07:55 UT but appeared suddenly one minute later at 07:56 UT.
176 At that time, a short spike of EUV emission projected out of the HXR emission zone.
177 The spike quickly transformed itself into a jet rooted at the non-thermal HXR source
178 region.

179 At 08:03 UT we could still find a faint trace of the HXR source and some remnant of
180 the EUV jet. By 08:11 UT everything was gone. In this eruption event, unlike those
181 analyzed by Krucker, et al. (2011), the topology does not show two or three
182 non-thermal sources and a thermal one, possibly because the sources were more
183 compact and hence spatially unresolved in the HXR images (resolution
184 ~6"). However, the EUV jet rooted in two opposite polarities with a cospatial
185 non-thermal source indicates a possibility for reconnection and the production of fast
186 escaping electrons. Figure 4 shows the time evolution of EUV AIA 94-, 131-, 211-,
187 and 304 Å intensities integrated along the path of the jet during the flare eruption. The
188 sudden appearance of the jet occurred at the same time as the impulsive phase flare at
189 07:58 UT. Besides the first jet, a second jet can be recognized at 08:00 UT in the AIA

190 211 Å image. Also shown is the Wind/WAVE spectrogram of the type-III radio burst.
191 The intensity enhancement of the first EUV jet was associated with the radio burst,
192 but the onset times were slightly different in the four filters. The onset of the slower
193 jet, seen in the 211-, 304 Å filters, lagged behind the type-III burst, but the faster jet,
194 observed in the 94- and 131 Å filters, preceded it by a few seconds. A similar short
195 delay between radio bursts and 211 Å jets was described by Innes, Cameron, and
196 Solanki (2011). They also noted that the EUV jet started beyond the brightening in the
197 footpoint area which is the configuration seen in this jet as well (figure 4). The second
198 jet was easily visible in the 211-, 304 Å images but not in the other two filters.
199 Furthermore, it was not associated with a HXR, 30-50 keV, source or a type-III radio
200 burst. This analysis of the time evolution shows that the onset of the first jet, which
201 was associated with a radio burst, was initially seen in 94- and 131 Å emission. The
202 second jet was neither seen in 94- and 131-Å emission nor was it associated with a
203 radio burst. This can help us to understand the formation of EUV jets and their
204 relation to the trigger of type-III bursts which will be discussed in the next section.

205 3.3 CORONAL TEMPERATURE DISTRIBUTIONS

206 To examine the formation of the EUV jet and its relationship with the production of
207 the type-III burst, we looked at the plasma temperature evolution in the vicinity of AR
208 11158, taking advantage of the high time resolution of SDO/AIA. The coronal
209 temperature was obtained from the differential emission measure (DEM) using data
210 from six EUV filters (94, 131, 171, 193, 211, 335) of AIA (Aschwanden et al. 2011)
211 and the references therein. In Figure 5, the deep blue region is the cool open-field area
212 in the AR 11158 main loop system while the orange region, on the right, is the higher
213 temperature closed-field area. To understand the temperature distribution and

214 evolution in the jet structure, a black contour outlines the jet shape as observed in the
215 211 Å images and white thick circles indicate the HXR sources at the time of the
216 temperature maps. For this discussion, we divide the time interval into two parts.

217 1. Before the type-III burst (07:55:50-07:57:26 UT)

218 Initially, the temperature of the low-lying emission at the site of the jet is about 1-2
219 MK. The temperature of the footpoint area started to rise as soon as the HXR source
220 appeared and increased until the onset of the type-III burst. From the previous section,
221 the footpoint brightening preceded the onset of the EUV jet, and here we find that this
222 early brightening was accompanied by a temperature increase. There was a complex
223 mixture of hot, warm and cool temperatures inside a cusp-like feature at the top of a
224 low-lying loop at the base of the jet. At the same time, the radio signal
225 drifted quickly from a few GHz to ~1 MHz (Figure 1) as the type-III-burst-associated
226 electron beams propagated outward. This complex structure might relate to the
227 production of type-III bursts but a more detailed analysis is required.

228 2. After the type-III burst (07:58:26-08:01:14 UT)

229 The temperature distribution along the jet was not homogeneous but segmental,
230 although most of the jet region was at the same temperature as its surroundings. The
231 footpoint area was always hotter while the HXR source was visible. When the second
232 jet started (08:00 UT), the temperature of the jet rose up temporarily but without any
233 correlated type-III burst. After the HXR sources vanished (08:05-08:10 UT), the jet
234 shrank and its temperature slowly decreased to that of the surroundings. At the same
235 time, the temperature of the low-lying loop also returned to its pre-radio-burst state.

236 In this temporal and spatial temperature analysis, we found that an early temperature

237 increase at the jet footpoints precedes the onset of the EUV jet and type-III burst
238 which is consistent with the early footpoint brightening in the EUV intensity-time plot.
239 This early temperature increase might be due to flare-accelerated electrons with
240 lower-energy (HXR source in 4-10 keV). The footpoint area sustained its high
241 temperature until a few minutes after the type-III burst which is unfavorable for the
242 production of the next type-III burst according to the simulation results of Li et al.
243 (2011). This might be the reason why there was no type-III burst during the second
244 X-ray emission peak (Figure 1). Another possibility, as discussed above, is that the
245 reconnection and acceleration process was not strong enough to produce a
246 non-thermal beam of electrons.

247 4. SUMMARY AND DISCUSSION

248 A comprehensive study has been carried out for the analysis of the interrelation
249 between the type III radio burst, EUV jets and HXR emissions of the first active
250 region of solar cycle 24, AR 11185, on 2011 February 15. From a consideration of the
251 timing and spatial locations, a common origin of the type III radio bursts, the EUV jet
252 and HXR source region can be well established. The new measurements by the
253 SDO/AIA instrument showed how the temperature of jet plasma distributes before
254 and after the type III radio burst occurs. Further investigations of the dynamics of
255 such EUV jets with observations from SDO, RHESSI and space-borne and
256 ground-based radio telescopes would bring new insights to the corresponding particle
257 energization and reconnection process.

258

259

260 5. Acknowledgment

261 We thank Bernard Jackson and Ya-Hui Yang for useful information and suggestions.

262 We also thank referees for many useful comments and suggestions. This work is
263 supported by NSC grant: NSC 96-2752-M-008-011-PAE and by the Ministry of
264 Education under the Aim for Top University Program, NCU.

265

266

267

268

269

270

271

272

273

274

275

276

277

278

279

280

281

282

283

284 References

- 285 Aschwanden, M. J., Boerner, P., Schrijver, C. J., & Malanushenko, A. 2011, *Sol.*
286 *Phys.*, 1
- 287 Aurass, H., Klein, K. L., & Martens, P. 1994, *Sol. Phys.*, 155, 203
- 288 Beauregard, L., Verma, M., & Denker, C. 2012, *Astronomische Nachrichten*, 333,
289 125
- 290 Benz, A. O., Grigis, P. C., Csillaghy, A., & Saint-Hilaire, P. 2005a, *Sol. Phys.*, 226,
291 121
- 292 Benz, A. O., Monstein, C., & Meyer, H. 2005b, *Sol. Phys.*, 226, 143
- 293 Benz, A. O., Monstein, C., Meyer, H., Manoharan, P. K., Ramesh, R., Altyntsev,
294 A., Lara, A., Paez, J., & Cho, K. S. 2009, *Earth, Moon, and Planets*, 104, 277
- 295 Bougeret, J., Goetz, K., Kaiser, M., Bale, S., Kellogg, P., Maksimovic, M., Monge,
296 N., Monson, S., Astier, P., & Davy, S. 2008, *Space Sci. Rev.*, 136, 487
- 297 Bougeret, J. L., Kaiser, M., Kellogg, P., Manning, R., Goetz, K., Monson, S.,
298 Monge, N., Friel, L., Meetre, C., & Perche, C. 1995, *Space Sci. Rev.*, 71, 231
- 299 Dąbrowski, B. P., & Benz, A. O. 2009, *A&A*, 504, 565
- 300 Innes, D., Cameron, R., & Solanki, S. 2011, *A&A*, 531, L13
- 301 Kahler, S., Aurass, H., Mann, G., & Klassen, A. 2007, *ApJ*, 656, 567
- 302 Klassen, A., Gómez-Herrero, R., & Heber, B. 2011, *Sol. Phys.*, 1
- 303 Krucker, S., Kontar, E. P., Christe, S., Glesener, L., & Lin, R. P. 2011, *ApJ*, 742, 82
- 304 Kundu, M., Nindos, A., Vilmer, N., Klein, K. L., Shibata, K., & Ohyama, M. 2001,
305 *ApJ*, 559, 443
- 306 Kundu, M., Raulin, J., Nitta, N., Hudson, H., Shimojo, M., Shibata, K., & Raoult,
307 A. 1995, *ApJ*, 447, L135
- 308 Kundu, M., Strong, K., Pick, M., White, S., Hudson, H., Harvey, K., & Kane, S.
309 1994, *ApJ*, 427, L59
- 310 Lemen, J. R., Title, A. M., Akin, D. J., Boerner, P. F., Chou, C., Drake, J. F.,
311 Duncan, D. W., Edwards, C. G., Friedlaender, F. M., & Heyman, G. F. 2012, *Sol.*
312 *Phys.*, 1
- 313 Li, B., Cairns, I. H., Yan, Y. H., & Robinson, P. A. 2011, *ApJ*, 738, L9
- 314 Lin, R. 1985, *Sol. Phys.*, 100, 537
- 315 Lin, R. P., Dennis, B. R., Hurford, G., Smith, D., Zehnder, A., Harvey, P., Curtis,
316 D., Pankow, D., Turin, P., & Bester, M. 2002, *Sol. Phys.*, 210, 3
- 317 Müller-Mellin, R., Böttcher, S., Falenski, J., Rode, E., Duvet, L., Sanderson, T.,
318 Butler, B., Johlander, B., & Smit, H. 2008, *Space Sci. Rev.*, 136, 363
- 319 Nitta, N. V., Mason, G. M., Wiedenbeck, M. E., Cohen, C. M. S., Krucker, S.,
320 Hannah, I. G., Shimojo, M., & Shibata, K. 2008, *ApJ*, 675, L125
- 321 Pick, M., Mason, G., Wang, Y. M., Tan, C., & Wang, L. 2006, *ApJ*, 648, 1247

322 Raulin, J., Kundu, M., Hudson, H., Nitta, N., & Raoult, A. 1996, A&A, 306, 299
323 Schou, J., Scherrer, P., Bush, R., Wachter, R., Couvidat, S., Rabello-Soares, M.,
324 Bogart, R., Hoeksema, J., Liu, Y., & Duvall, T. 2012, Sol. Phys., 1
325 Shibata, K., Ishido, Y., Acton, L. W., Strong, K. T., Hirayama, T., Uchida, Y.,
326 McAllister, A. H., Matsumoto, R., Tsuneta, S., & Shimizu, T. 1992, PASJ, 44, L173
327 Shibata, K., Shimojo, M., Yokoyama, T., & Ohyama, M. 1997. Theory and
328 observations of x-ray jets, 29
329 Shimojo, M., Hashimoto, S., Shibata, K., Hirayama, T., Hudson, H. S., & Acton, L.
330 W. 1996, PASJ, 48, 123
331 Shimojo, M., Shibata, K., & Harvey, K. L. 1998, Sol. Phys., 178, 379
332 Suzuki, S., & Dulk, G. 1985, Solar Radiophysics: Studies of Emission from the
333 Sun at Metre Wavelengths, 1, 289
334 Tan, B., Yan, Y., Tan, C., Sych, R., & Gao, G. 2012, ApJ, 744, 166
335 Wang, Y. M., Pick, M., & Mason, G. 2006, ApJ, 639, 495
336
337

338

339

340

341

342

343

344

345

346

347

348

349

350

351

352 Figure Captions

353

354 Figure 1. A comparison of the Type-III radio burst at different frequency ranges
355 associated with AR 11158 at UT 07:58 on February 15, 2011. From top to bottom:
356 Phoenix 3, Bleien, Ooty, Wind/Waves.

357

358 Figure 2. A comparison of the Type-III radio burst at 07:58 UT on February 15, 2011,
359 with the HXR fluxes at 4-10 keV, 10-30 keV and 30-50 keV from RHESSI, and the
360 EUV intensities at AIA 94, 131, 211, and 304Å .

361

362 Figure 3(a) A map of AR 11158 obtained by AIA 211 Å at UT 07:58 on February 15,
363 2011 is superimposed over HMI magnetogram. The magnetic field strength contours
364 are divided in intervals of 95%, 80%, 60%, and 40% of the maximum values. The
365 positive polarity is denoted by blue and the negative polarity in red. A clear jet feature
366 appears on the left –hand side of the AR near the boundary.

367 (b) Time evolution of the EUV jet and the HXR source region of AR 11158 is in the
368 time interval between 07:55 UT and 08:11 UT on February 15, 2011. RHESSI HXR
369 images are reconstructed by the CLEAN algorithm using front segments of detectors
370 3 through 8. And the HXR contours are divided in intervals of 90%, 70%, and 50% of
371 the maximum values. The green line is for 4-10 keV channel, blue for 10-30 keV and
372 purple for 30-50 keV. The box with dashed lines outlines the area for summing count
373 rates which are presented in Figure 4.

374

375 Figure 4 A integrated EUV intensity profile along the jet direction obtained by
376 summing the count rates in the box as shown in the inset of Figure 3b. The images

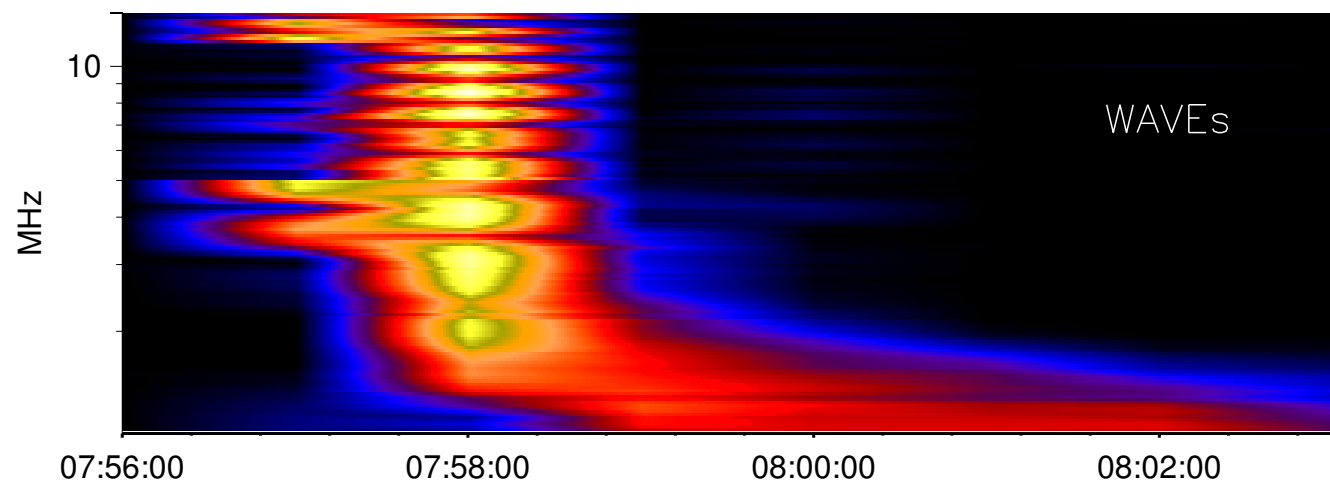
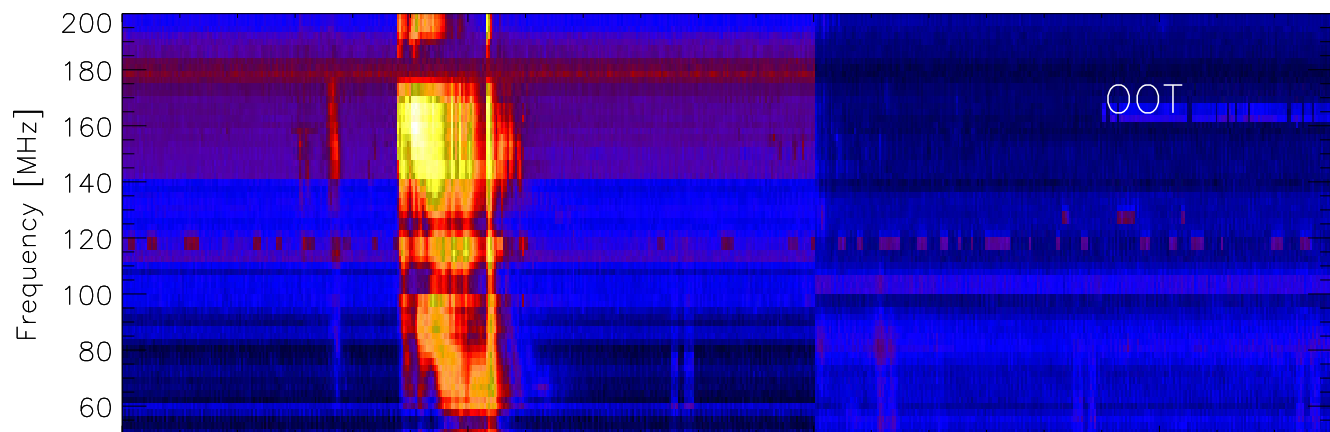
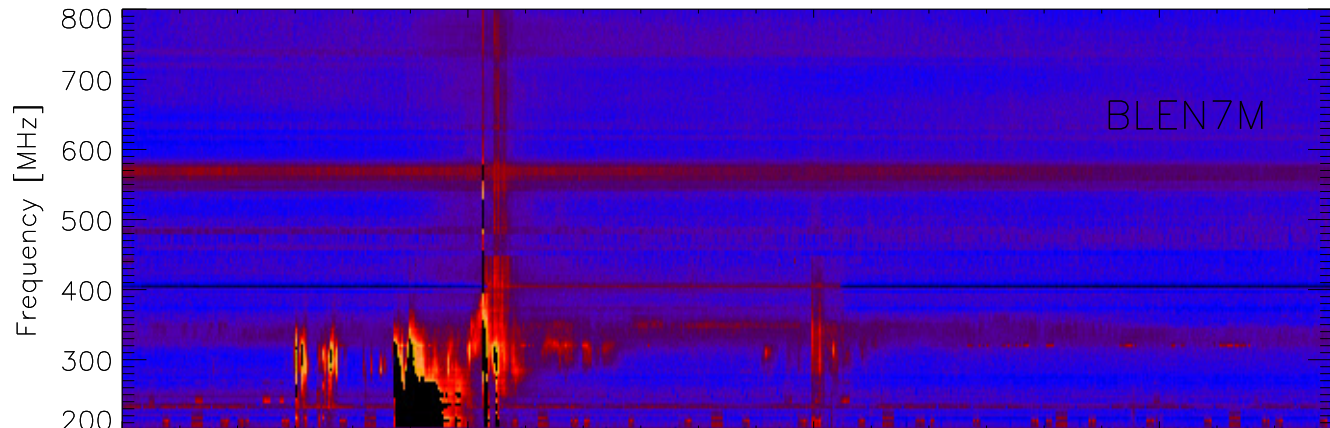
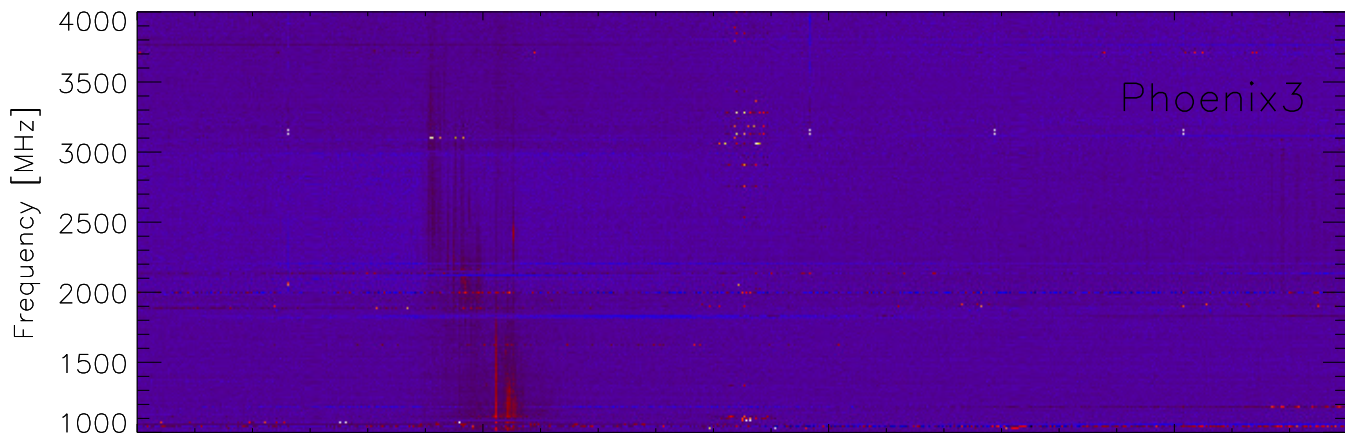
377 from top to bottom: 94, 131, 211, 304 Å and with the Wind/Waves radio dynamic
378 spectrum. The white line with the arrow head marks the loop top position.

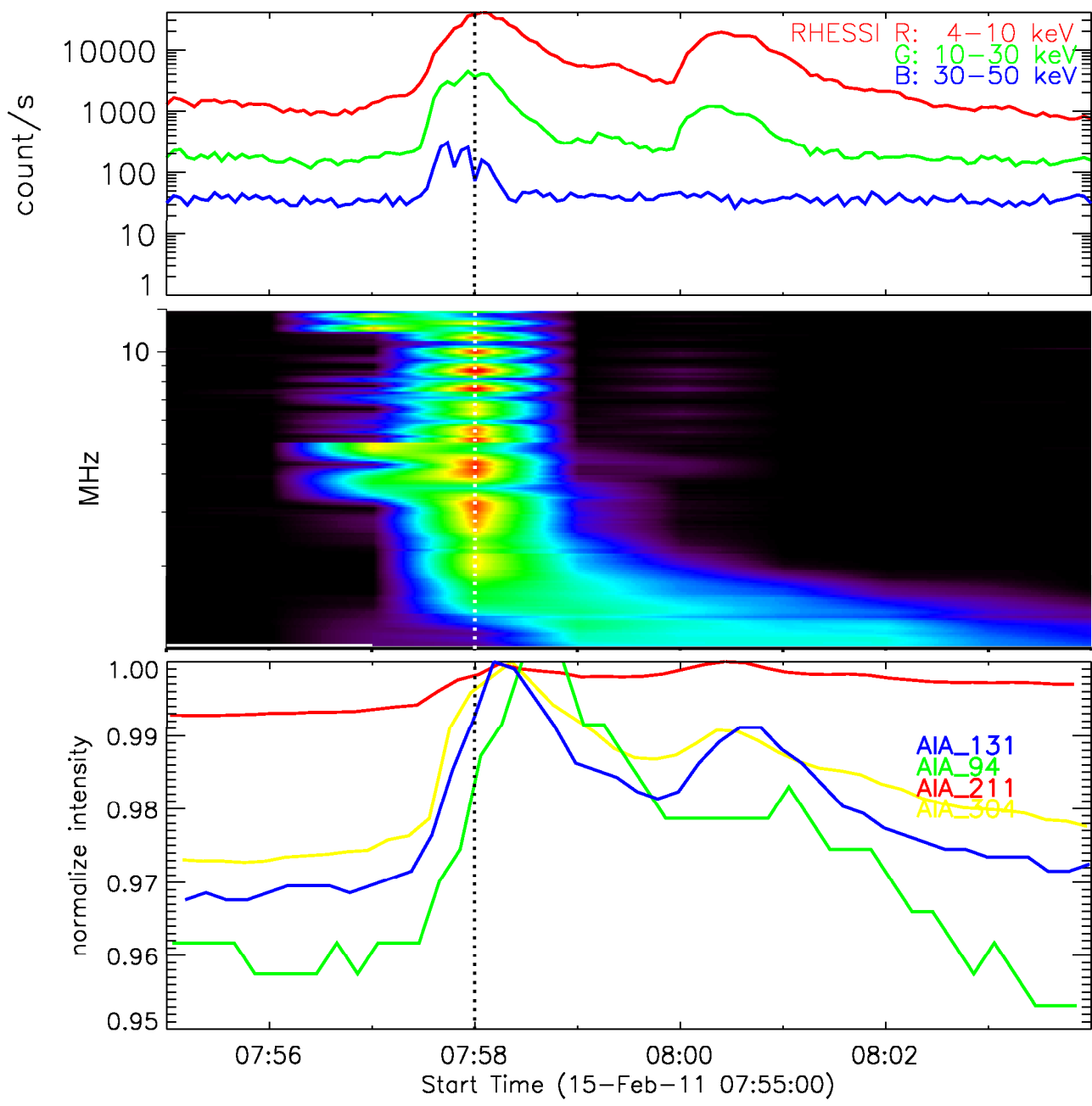
379

380 Figure 5 Time evolution of the coronal temperature obtained from a differential
381 emission measure (DEM) analysis of AR 11158 between 07:55 UT and 08:10 UT on
382 February 15, 2011. The temperature range is indicated in the color bar on the right
383 side of image (07:55 UT), $\log(T) = 5.7-7$ ($T \sim 0.5-10$ MK). The white contour marks
384 the HXR sources in interval of 70%, 90% of maximum values. The black contour
385 outlines the jet shape as observed in the associated 211 Å images.

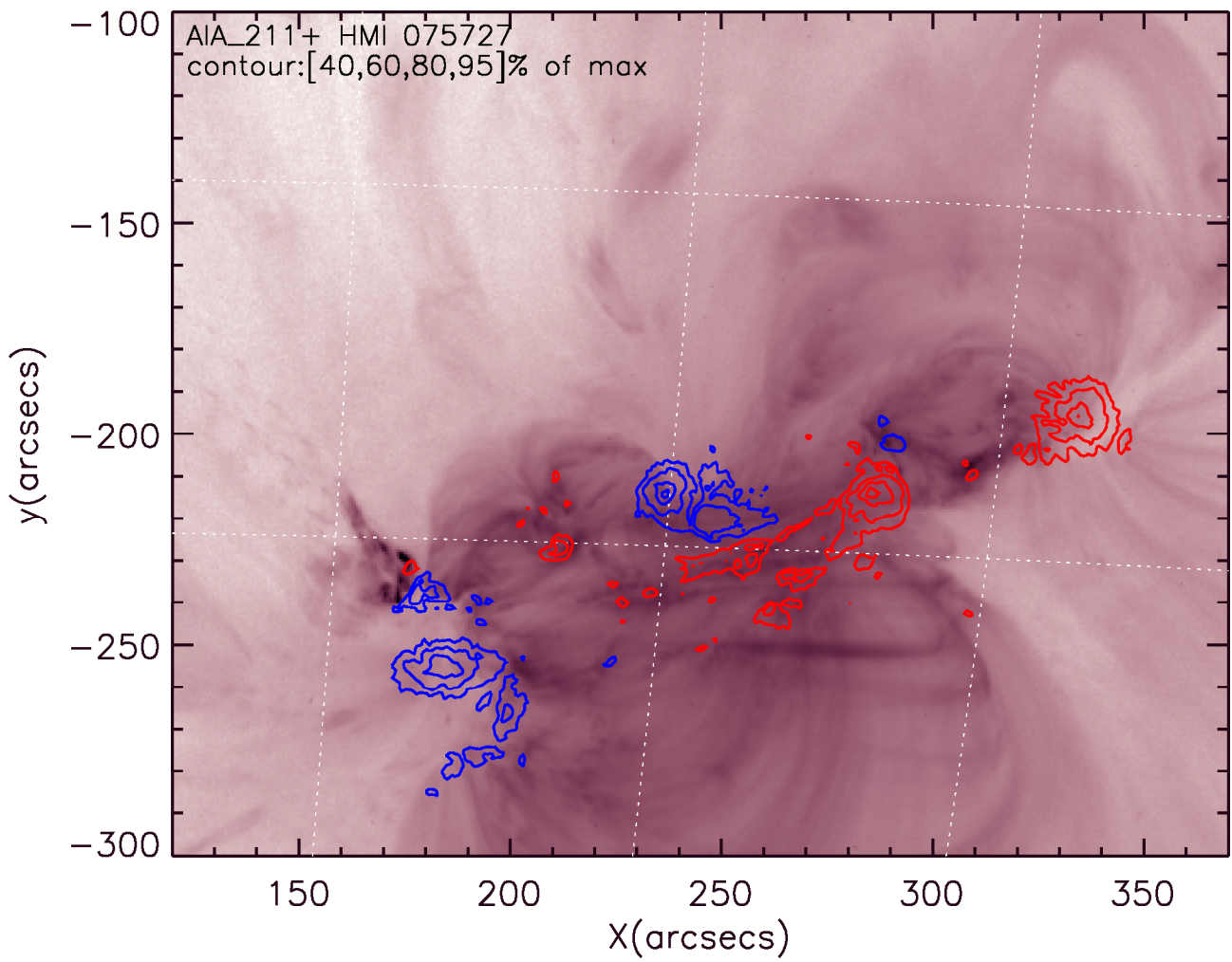
386

387

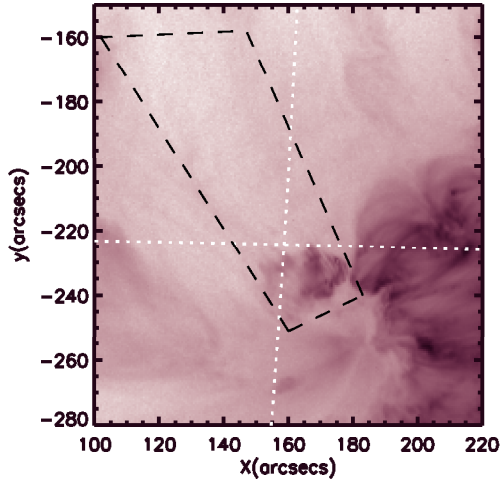




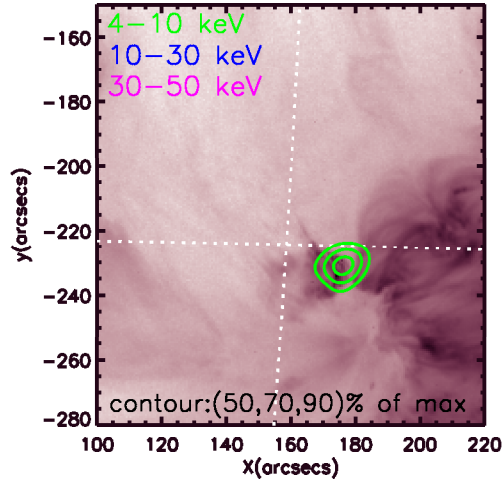
15-Feb-2011_075712



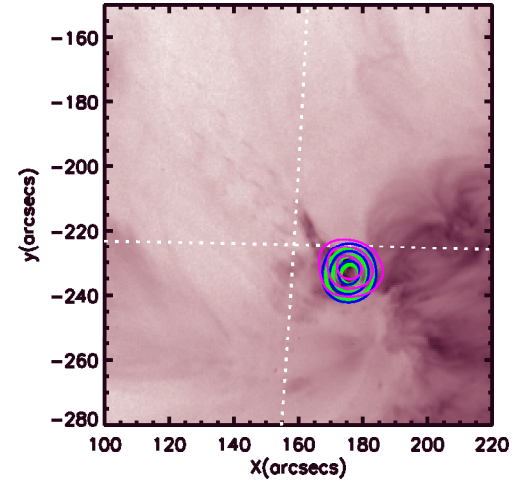
075548



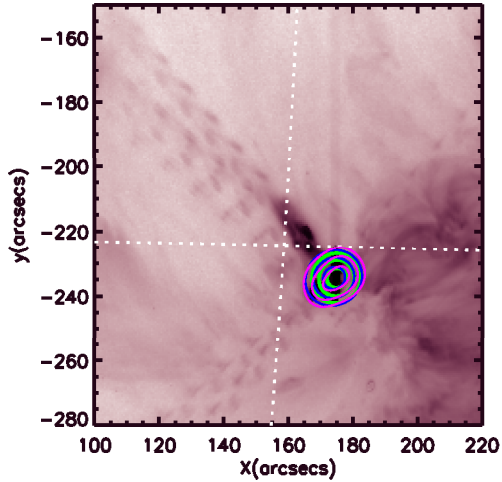
075636



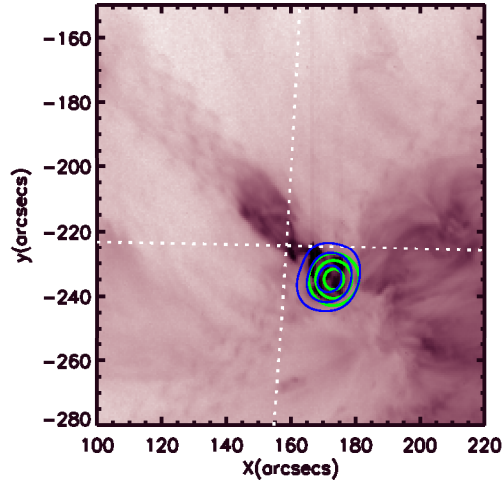
075712



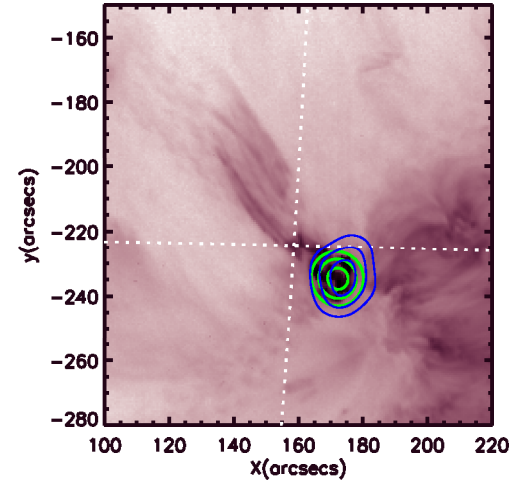
075748



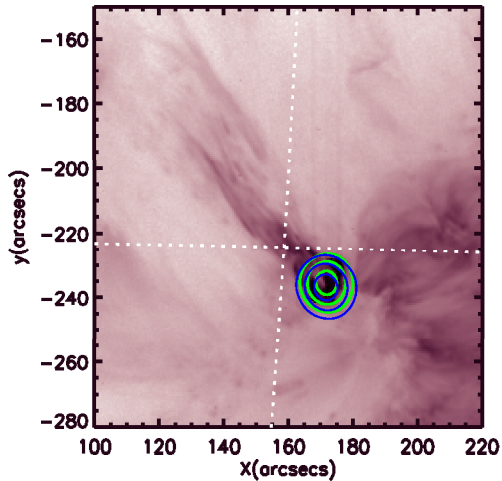
075836



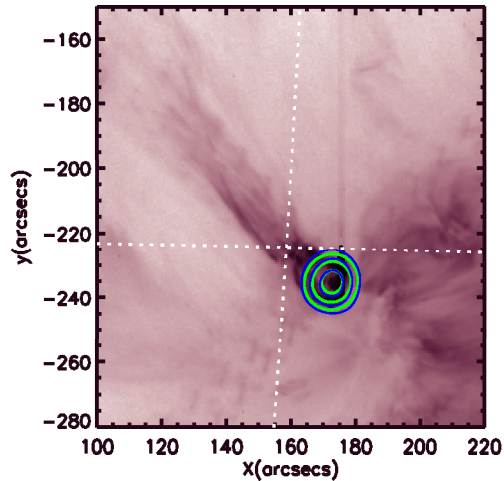
075912



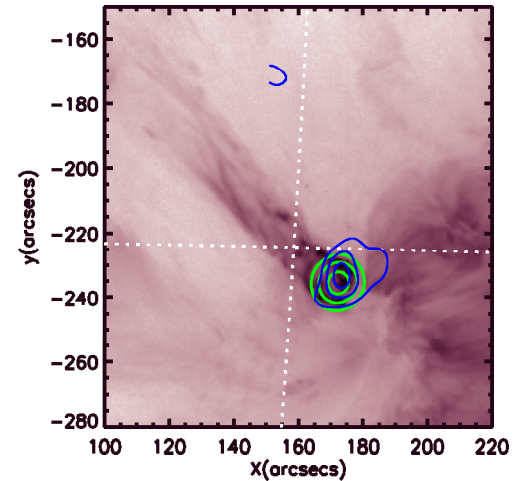
075948



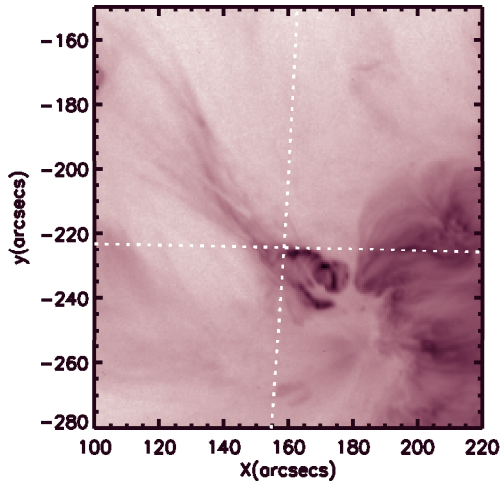
080036



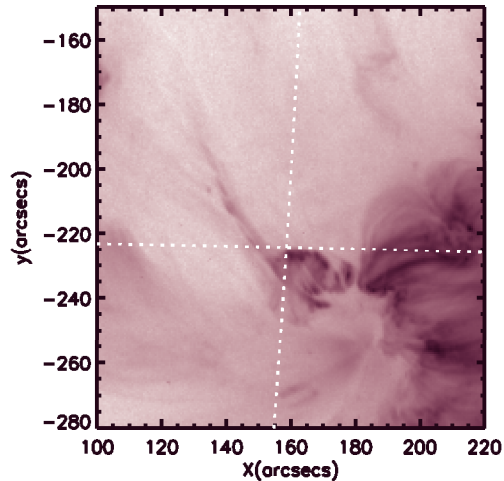
080112



080348



080700



081000

